



# Full solar spectrum photocatalytic oxygen evolution by carbon-coated TiO<sub>2</sub> hierarchical nanotubes

Zhangqian Liang<sup>a</sup>, Xiaojuan Bai<sup>a</sup>, Pin Hao<sup>b</sup>, Yichen Guo<sup>a</sup>, Yanjun Xue<sup>a</sup>, Jian Tian<sup>a,\*</sup>,  
Hongzhi Cui<sup>a,\*</sup>

<sup>a</sup> School of Materials Science and Engineering, Shandong University of Science and Technology, Qingdao 266590, China

<sup>b</sup> College of Chemistry, Chemical Engineering and Materials Science, Collaborative Innovation Center of Functionalized Probes for Chemical Imaging in Universities of Shandong, Key Laboratory of Molecular and Nano Probes, Ministry of Education, Shandong Normal University, Jinan 250014, China

## ARTICLE INFO

### Keywords:

Hierarchical nanotube  
Carbon coating  
O<sub>2</sub> evolution  
Photocatalysis  
Full solar spectrum

## ABSTRACT

Smart architectures of TiO<sub>2</sub> are attracting increasing attention due to their outstanding properties in a broad range of fields. Herein, hierarchical TiO<sub>2</sub> nanotube with uniform carbon coatings is synthesized as the full solar spectrum photocatalytic materials for O<sub>2</sub> evolution by a facile solvothermal method. This unique structure consists of an interstitial hollow spaces and a functional nanotube shell assembled from two-dimensional (2D) nanosheets. By adjusting the types of solvents and reaction time, the morphologies of TiO<sub>2</sub>/C composites can be tuned to nanoparticles, nanorods, or hierarchical nanotubes. Among these morphologies, the TiO<sub>2</sub>/C hierarchical nanotube exhibits the best photocatalytic activity and favorable stability toward oxygen evolution from water oxidation under full solar spectrum light irradiation. The reason is attributed to the desirable incorporation of visible/near-infrared (NIR) light active carbon coating with UV light responsive TiO<sub>2</sub> for promoted solar energy utilization. Besides, the solvothermal step leads to hierarchical nanotube structures which can generate multiple reflections of incident light so as to promote an efficient light harvesting due to an enhanced specific surface area (244.4 m<sup>2</sup> g<sup>-1</sup>) and light scattering ability. Moreover, the generated carbon coatings on the surface of TiO<sub>2</sub> facilitate electron-hole separation.

## 1. Introduction

Photocatalytic water splitting constructing by the reduction of protons to H<sub>2</sub> and oxidation of water to O<sub>2</sub> is one of the most promising ways to convert solar energy into green and renewable energy, which is expected to meet the rising global energy demand in future [1–6]. However, the half-reaction of water oxidation is a chemist's nightmare, in that it involves complex four-electrons redox process and high activation energy for O–O bond formation [7]. Therefore, the development of highly efficient water splitting oxidation catalysts (WOCs) has become especially important for the conversion of sunlight into green and accumulation chemical energy [8]. The photocatalytic performance of materials is highly dependent on their structures [9]. Smaller particle size and some specific morphologies, in which the electron diffusion distance is shortened, can improve the photocatalytic activity [10]. Several morphologies have been extensively investigated including nanotubes [11–13], nanowires [14,15], hollow spheres [16,17], core@-shell [18,19] and yolk@shell [20,21] architectures. In particular, complex 1D hollow tube nanostructures offer exciting opportunities in

photocatalysis. These structures generally include a 1D skeleton and a hollow porous shell, which display an improved light harvesting activity because of their larger specific surface areas and light-scattering abilities.

As an excellent semiconductor material, TiO<sub>2</sub> has a good application in the field of photocatalytic water splitting to produce H<sub>2</sub> and O<sub>2</sub> [22–26]. In particular, rutile TiO<sub>2</sub> powder possesses unique photocatalytic properties for water oxidation [27]. Despite a great deal of research, rutile TiO<sub>2</sub> photocatalysts are not appropriate for the visible or even full solar spectrum-light-induced water splitting because of poor light utilization. In addition, the fast recombination rate of photoexcited electron-hole pairs generated by unfavorable structure greatly limits their practical applications, which is an urgent problem to be solved as well. Therefore, to satisfy the requirements of water splitting, the development of new materials or methodologies to obtain efficient photocatalysts with advantage of extended light response and an improved electron-hole separation efficiency remains a tremendous challenge.

It should be noted that the introduction of carbon coating into TiO<sub>2</sub>

\* Corresponding authors.

E-mail addresses: [tj6891011@163.com](mailto:tj6891011@163.com) (J. Tian), [cuihongzhi1965@163.com](mailto:cuihongzhi1965@163.com) (H. Cui).

<https://doi.org/10.1016/j.apcatb.2018.11.017>

Received 23 August 2018; Received in revised form 28 October 2018; Accepted 5 November 2018

Available online 08 November 2018

0926-3373/ © 2018 Elsevier B.V. All rights reserved.

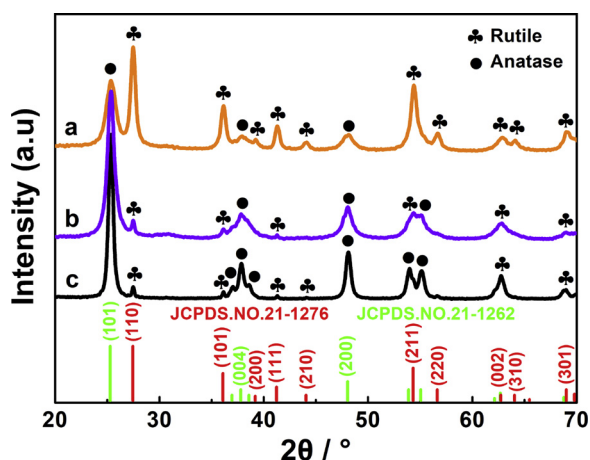


Fig. 1. XRD patterns of (a)  $\text{TiO}_2/\text{C}$  HNTs, (b)  $\text{TiO}_2/\text{C}$  NRs and (c)  $\text{TiO}_2/\text{C}$  NPs.

can adjust the band gap structures and even broaden the absorption range from UV to visible or even near-infrared (NIR) region [28]. Besides, the photogenerated electron transfer can be significantly speeded up due to the high electric conductivity of carbon coatings [29]. The hybridization of hierarchical  $\text{TiO}_2$  hollow nanotubes with carbon coatings would provide an effective way to enhance the charge separation and photocatalytic efficiency. In this regard, the resulting carbon coated hierarchical  $\text{TiO}_2$  nanotubes would possess the following advantages: (i) prominent full sunlight utilization will be achieved owing to the combination of visible and NIR-light-active carbon coatings and UV-light-responsive  $\text{TiO}_2$ ; (ii) the hierarchical structure with carbon coatings enables convenient charge and light-scattering abilities, which would promote the separation of photoinduced electron-

hole pair and display an improved light harvesting activity.

In this work, we investigated a series of  $\text{TiO}_2/\text{C}$  composites such as carbon coated hierarchical  $\text{TiO}_2$  nanotubes ( $\text{TiO}_2/\text{C}$  HNTs), carbon coated  $\text{TiO}_2$  nanorods ( $\text{TiO}_2/\text{C}$  NRs) and carbon coated  $\text{TiO}_2$  nanoparticles ( $\text{TiO}_2/\text{C}$  NPs) via a solvothermal method through the adjusting the types of solvents and reaction time. Among these morphologies,  $\text{TiO}_2/\text{C}$  HNTs show full solar spectrum response, higher specific surface area ( $244.4 \text{ m}^2 \text{ g}^{-1}$ ), longer fluorescence lifetime, and lower photo-generated carrier recombination efficiency. Benefiting from the unique structural feature and outstanding property, the as-obtained  $\text{TiO}_2/\text{C}$  HNTs exhibit an extraordinarily high photocatalytic oxygen evolution activity and favorable stability upon full solar spectrum light illumination.

## 2. Experimental section

### 2.1. Synthesis of carbon coated hierarchical $\text{TiO}_2$ nanotubes ( $\text{TiO}_2/\text{C}$ HNTs)

In a typical synthesis, 1.0 g of  $\text{TiOSO}_4$  was added into mixed solvents containing glycerol, ethanol, and ethyl ether in a volume ratio of 1:2:1. After being stirred for 0.5 h, the mixed suspension was transferred into a 100 mL Teflon-coated autoclave and heat treated at  $120^\circ\text{C}$  for 24 h. The as-prepared precipitates were separated by suction filtration, and washed thoroughly with deionized water and ethanol several times, and then dried at  $80^\circ\text{C}$  for 12 h under vacuum. Finally, the obtained products were annealed at  $700^\circ\text{C}$  for 2 h in an  $\text{Ar}/\text{H}_2$  atmosphere at a ramping rate of  $5^\circ\text{C min}^{-1}$  to form  $\text{TiO}_2/\text{C}$  HNTs material. For comparison, carbon-coated  $\text{TiO}_2$  nanorods ( $\text{TiO}_2/\text{C}$  NRs) were prepared by the aforementioned method without adding the glycerol solvent, and carbon-coated  $\text{TiO}_2$  nanoparticles ( $\text{TiO}_2/\text{C}$  NPs) were prepared with only ethanol as the solvent.

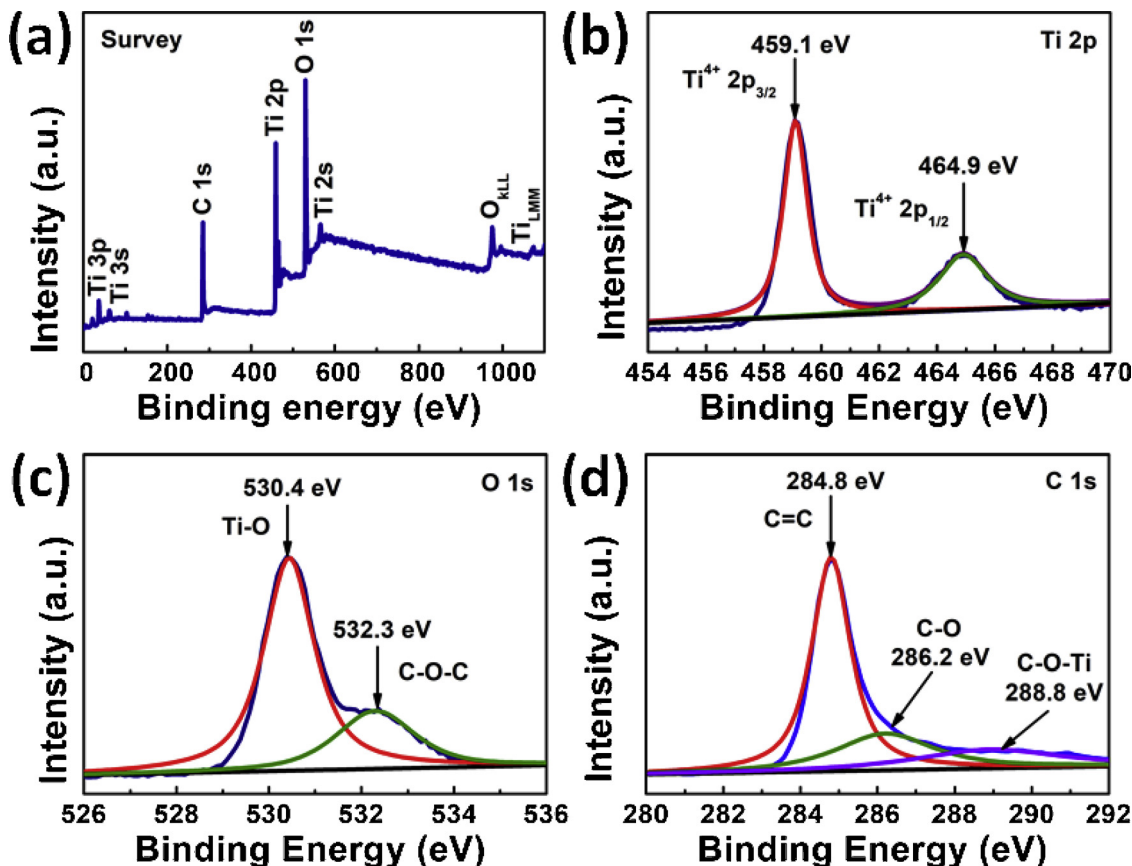


Fig. 2. (a) Survey, (b) Ti 2p, (c) O 1s, and (d) C 1s XPS spectra of  $\text{TiO}_2/\text{C}$  HNTs.

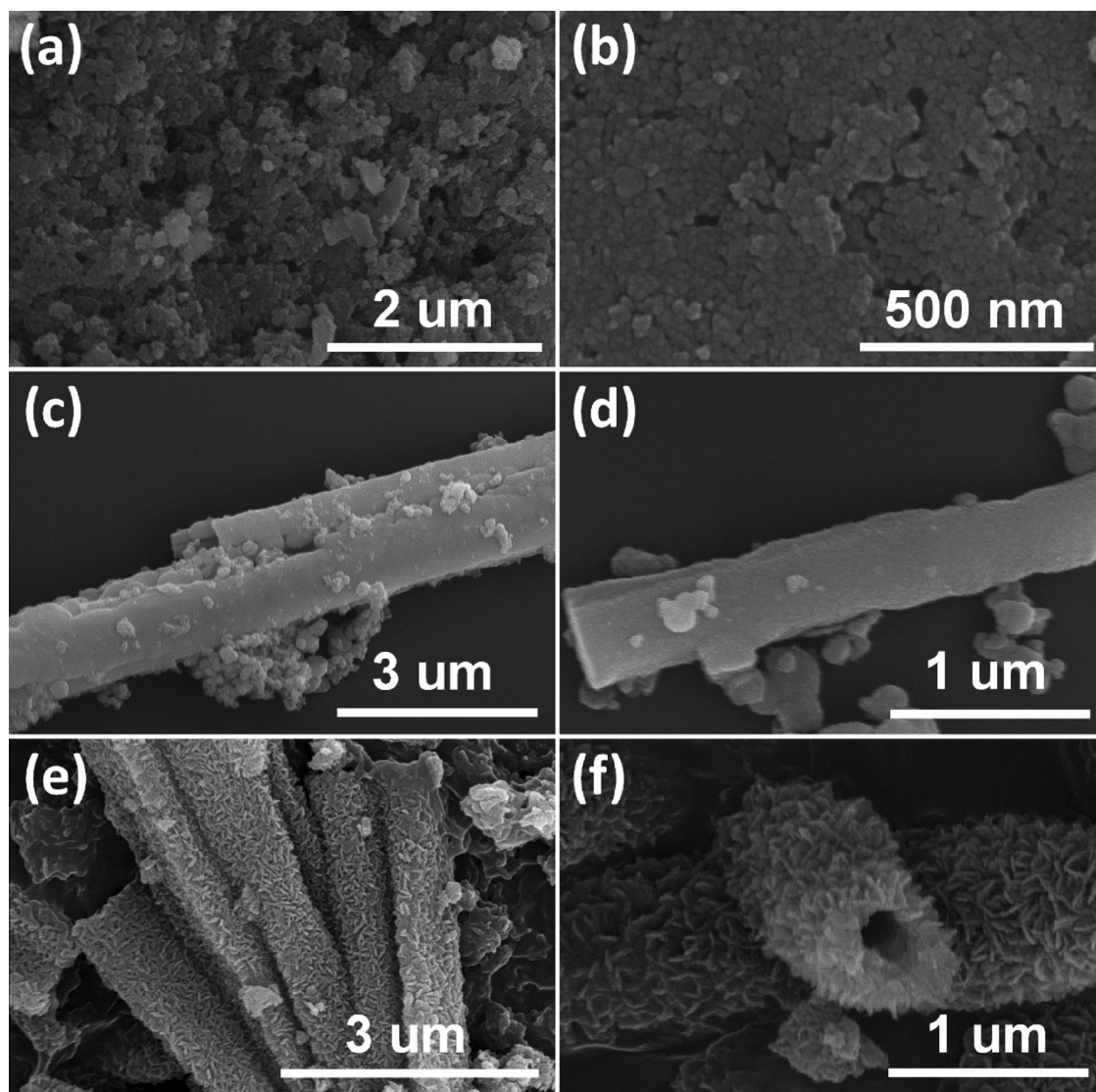


Fig. 3. SEM images of (a, b)  $\text{TiO}_2/\text{C}$  NPs, (c, d)  $\text{TiO}_2/\text{C}$  NRs, and (e, f)  $\text{TiO}_2/\text{C}$  HNTs.

## 2.2. Characterization

X-ray diffraction (XRD) measurements were collected on a D/Max2500PC X-ray diffractometer with  $\text{Cu-K}\alpha 1$  radiation ( $\lambda = 1.5418 \text{ \AA}$ ) operated at 40 kV. Scanning electron microscopy (SEM) was conducted on a FEI NANO SEM 450. This instrument included capability for element mapping with energy dispersive X-ray spectroscopy (EDX). Transmission electron microscopy (TEM) and high resolution TEM (HRTEM) were performed on a FEU G20 transmission electron microscope with an accelerating voltage of 200 kV. X-ray photoelectron spectroscopy (XPS) was carried out with a Thermo ESCALAB 250Xi spectrometer using Al  $\text{K}\alpha$  radiation at a voltage of 1486.6 eV and calibrated with the C 1s binding energy of 284.8 eV. The XPS results were deconvoluted with XPSPEAK software. The Brunauer-Emmett-Teller (BET) specific surface area measurements were carried out by  $\text{N}_2$  adsorption at 77 K using a Quadrasorb EVO apparatus with prior out gassing of the sample overnight at 200 °C under a primary vacuum. UV-vis-NIR absorption spectra of the materials were recorded on a UV-3101PC spectrophotometer. Transient photoluminescence curves of the as-prepared samples were obtained on a FLS980 Series of fluorescence lifetime spectrophotometer.

## 2.3. Photocatalytic and photoelectrochemical activity test

The photocatalytic activity of the prepared samples was evaluated toward the oxygen evolution in a quartz reactor containing 100 mL of deionized water in the presence of sacrificial agent. The photocatalytic tests were performed with 20 mg of catalyst dispersed with a mechanical stirring and argon was used as a carrier gas. Deionized water was used as oxygen source and silver nitrate (0.01 M) was added as sacrificial agent and electron acceptors in order to exclusively study the  $\text{O}_2$  evolution reaction. The 300 W Xe arc lamp with an AM-1.5 and UVIRCUT800 filter was used as simulated solar light and NIR light source, respectively. The reaction products were analyzed on-line by thermal conductivity detectors on a microgas chromatography GC-7920 instruments. The photocurrent response and electrochemical impedance of the samples were tested by using an electrochemical workstation (Shanghai Chenhua CHI660D) in a three-electrode system, in which the sample electrode is used as the photocathode, SEC as the reference electrode, a Pt wire as the counter electrode, 0.5 M  $\text{Na}_2\text{SO}_4$  aqueous solution as the electrolyte. The 500 W Xe arc lamp with an AM-1.5 filter was used as the light source. The apparent quantum efficiency (AQE) was measured under similar photocatalytic reaction condition except that a 300 W Xe arc lamp with a UVIRCUT420 filter was used as light source. The focused intensity for 300 W Xe arc lamp with a



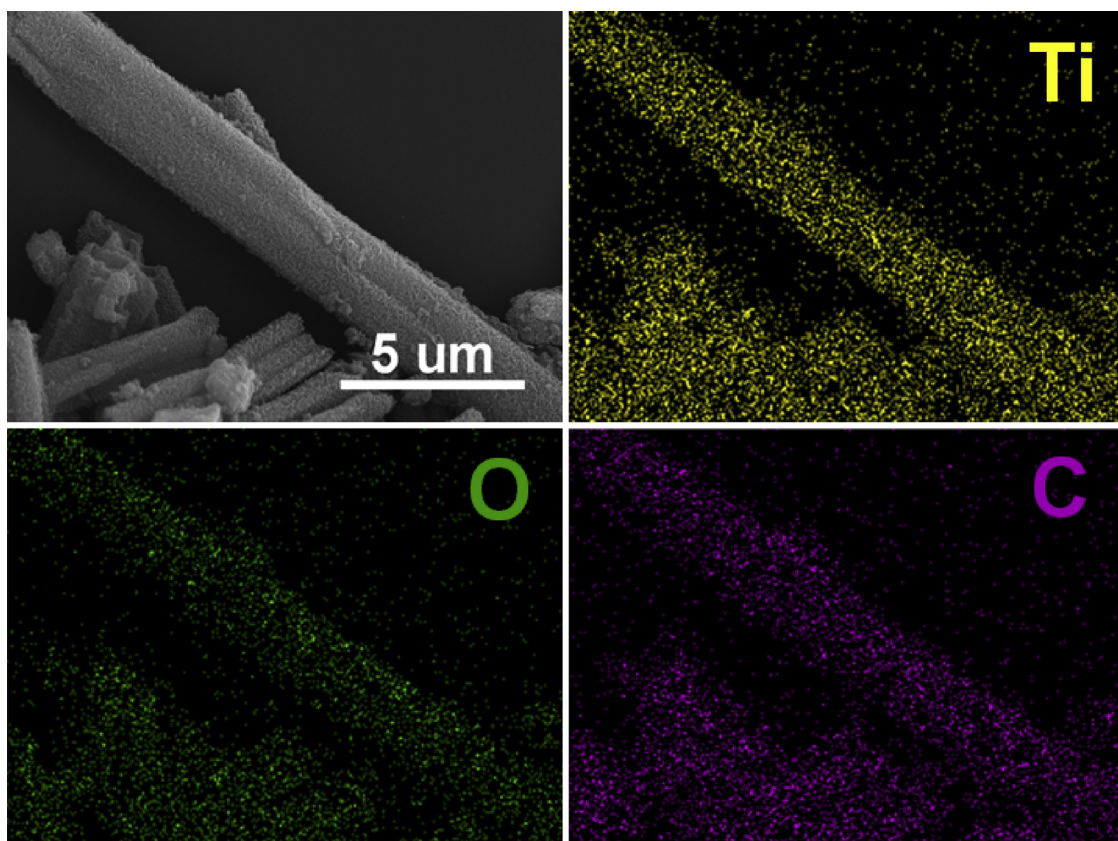


Fig. 4. Energy dispersive X-ray spectroscopy (EDX) mapping images of TiO<sub>2</sub>/C HNTs.

UVIRCUT420 filter was ca. 570.9 W/m<sup>2</sup>. The apparent quantum efficiency (AQE) was measured and calculated according to equation:

$$\text{AQE} = \frac{\text{number of reacted electrons}}{\text{number of incident photons}} \times 100$$

$$= \frac{\text{number of evolved O}_2 \text{ molecules} \times 4}{\text{number of incident photons}} \times 100\% \quad (1)$$

### 3. Results and discussion

The phase information was characterized through powder X-ray diffraction (XRD) measurement. The XRD patterns of as-prepared TiO<sub>2</sub>/C HNTs, TiO<sub>2</sub>/C NRs and TiO<sub>2</sub>/C NPs samples are depicted in Fig. 1. In curve a, the diffraction peaks at  $2\theta = 25.28^\circ$ ,  $37.80^\circ$  and  $48.05^\circ$  are assigned to the (101), (004) and (200) crystal planes of anatase TiO<sub>2</sub> (JCPDS No. 21-1272). The diffraction peaks at  $2\theta = 27.45^\circ$ ,  $36.09^\circ$ ,  $39.19^\circ$ ,  $41.23^\circ$ ,  $44.05^\circ$ ,  $54.32^\circ$ ,  $56.64^\circ$ ,  $62.74^\circ$ ,  $64.04^\circ$  and  $69.01^\circ$  are attributed to (110), (101), (200), (111), (210), (211), (220), (002), (310) and (301) crystal planes for rutile TiO<sub>2</sub> (JCPDS No. 21-1276). It indicates that the as-prepared TiO<sub>2</sub>/C HNTs have mixed phases with rutile being the dominant one according to the relatively higher intensity of its diffraction peaks. In curve b and c, the diffraction peaks of TiO<sub>2</sub>/C NRs and TiO<sub>2</sub>/C NPs can also be indexed to anatase TiO<sub>2</sub> (JCPDS No.21-1272) and rutile TiO<sub>2</sub> (JCPDS No.21-1276). However, anatase is the dominant in the as-prepared TiO<sub>2</sub>/C NRs and TiO<sub>2</sub>/C NPs, which is different from TiO<sub>2</sub>/C HNTs. It is generally believed that the rutile phase of TiO<sub>2</sub> is better for water oxidation, which is useful for oxygen evolution [27]. Thus, TiO<sub>2</sub>/C HNTs with rutile as dominant phase will possess better photocatalytic properties for water oxidation.

The TG curves in Fig. S1 indicate the carbon amounts of the three samples. The carbon amounts in TiO<sub>2</sub>/C NPs and TiO<sub>2</sub>/C NRs are 3.3% and 1.1%, respectively. Apart from the weight loss of about 0.5% below 200 °C due to the elimination of the adsorbed water molecules [30], the

carbon amount in TiO<sub>2</sub>/C HNTs is about 14.8%. The high carbon amount of TiO<sub>2</sub>/C HNTs derives from the carbonization of residual organic solvent (glycerol in this situation) absorbed on the TiO<sub>2</sub> precursor surface during the calcination process [31].

To better understand the interaction between carbon coatings and TiO<sub>2</sub>, X-ray photoelectron spectroscopy (XPS) of TiO<sub>2</sub>/C HNTs, TiO<sub>2</sub>/C NRs and TiO<sub>2</sub>/C NPs was performed. The survey spectrum of TiO<sub>2</sub>/C HNTs, TiO<sub>2</sub>/C NPs and TiO<sub>2</sub>/C NRs in Figs. 2a, S2a and S3a indicates the existence of the elements of Ti, O, and C. The Ti 2p peaks at 459.1 and 464.9 eV are characteristic of the Ti 2p<sub>3/2</sub> and Ti 2p<sub>1/2</sub> energies of Ti<sup>4+</sup> in TiO<sub>2</sub> by observing the Ti 2p spectrum of TiO<sub>2</sub>/C HNTs, TiO<sub>2</sub>/C NPs and TiO<sub>2</sub>/C NRs in Figs. 2b, S2b and S3b [24]. The O 1s signals of TiO<sub>2</sub>/C HNTs, TiO<sub>2</sub>/C NRs and TiO<sub>2</sub>/C NPs (Figs. 2c, S2c and S3c) can be divided into two resolved peaks at 530.4 eV and 532.3 eV, which result from Ti–O and C–O–C bonds, respectively [32]. The C 1s peaks of TiO<sub>2</sub>/C HNTs, TiO<sub>2</sub>/C NPs and TiO<sub>2</sub>/C NRs (Figs. 2d, S2d and S3d) at 284.8, 286.2, and 288.8 eV in the high resolution XPS can be assigned to C=C, C–O, and C–O–Ti bonds, respectively [32]. The strong electronic coupling between carbon coatings and TiO<sub>2</sub> would probably accelerate the electron-hole separation.

SEM measurements were conducted to examine the morphologies of the as-prepared three samples (Fig. 3). When only ethanol as the solvent is added, the TiO<sub>2</sub>/C NPs show nanoparticle morphology with an average particle size of ~50 nm (Fig. 3a and b). After adding ethyl ether and ethanol in a volume ratio of 1:2, the morphology of TiO<sub>2</sub> turns into nanorods (TiO<sub>2</sub>/C NRs) (Fig. 3c and d). Interestingly, when glycerol, ethanol, and ethyl ether with a volume ratio of 1:2:1 are added, a hierarchical nanotube morphology with two open ends is formed (TiO<sub>2</sub>/C HNTs) (Fig. 3e). High magnification micrographs (Fig. 3f) further confirm the clearly visible presence of hierarchical nanosheets assemble on the surfaces of nanotubes. SEM energy dispersive X-ray spectroscopy (EDX) mapping was performed on TiO<sub>2</sub>/C HNTs sample to clarify the uniform distribution of Ti, O, and C

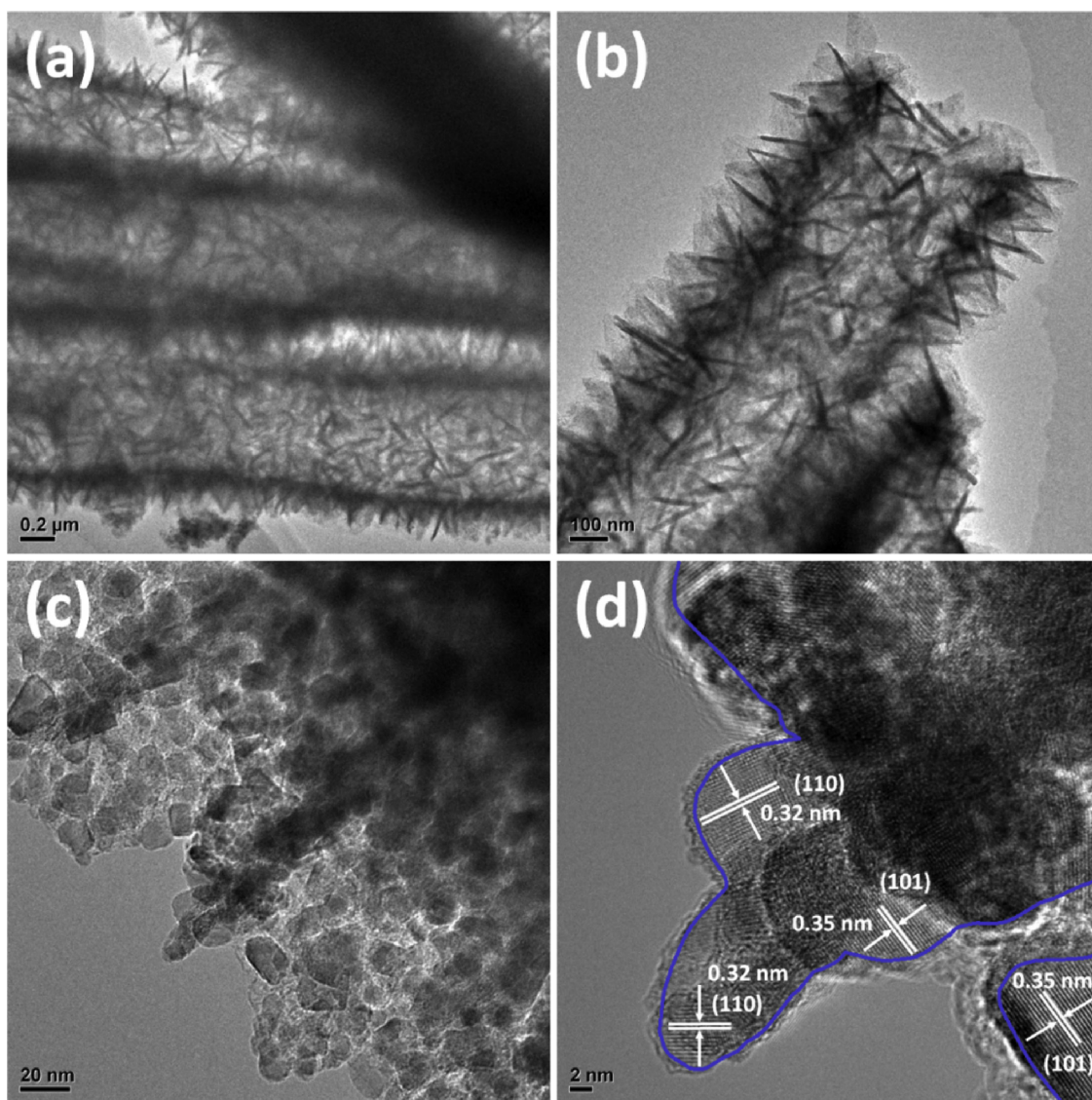
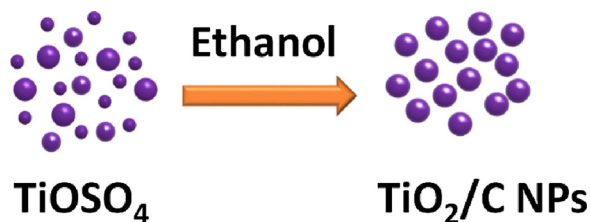


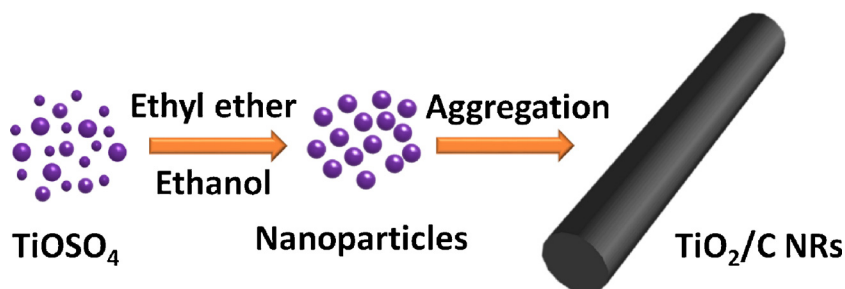
Fig. 5. (a–c) TEM and (d) HRTEM images of  $\text{TiO}_2/\text{C}$  HNTs.



Scheme 1. Schematic diagram of the evolution of  $\text{TiO}_2/\text{C}$  NPs.

throughout the nanotube (Fig. 4).

The transmission electron microscopy (TEM) images (Fig. 5a and b) of  $\text{TiO}_2/\text{C}$  HNTs confirm a nanotube structure of an interstitial hollow space ( $\sim 300$  nm in diameter) and nanotube shell. The nanotube shell is assembled from 2D nanosheets with a thickness of several tens of nanometers. A closer inspection of TEM image (Fig. 5c) indicates that the interwoven nanosheets in the hierarchical microtube shell compose of numerous crystallines with 5–10 nm in dimension. Clearly, these  $\text{TiO}_2$  nanoparticles loosely contact each other and thus give rise to abundant porous structures, which increases the specific surface area of



Scheme 2. Schematic diagram of the evolution of  $\text{TiO}_2/\text{C}$  NRs.



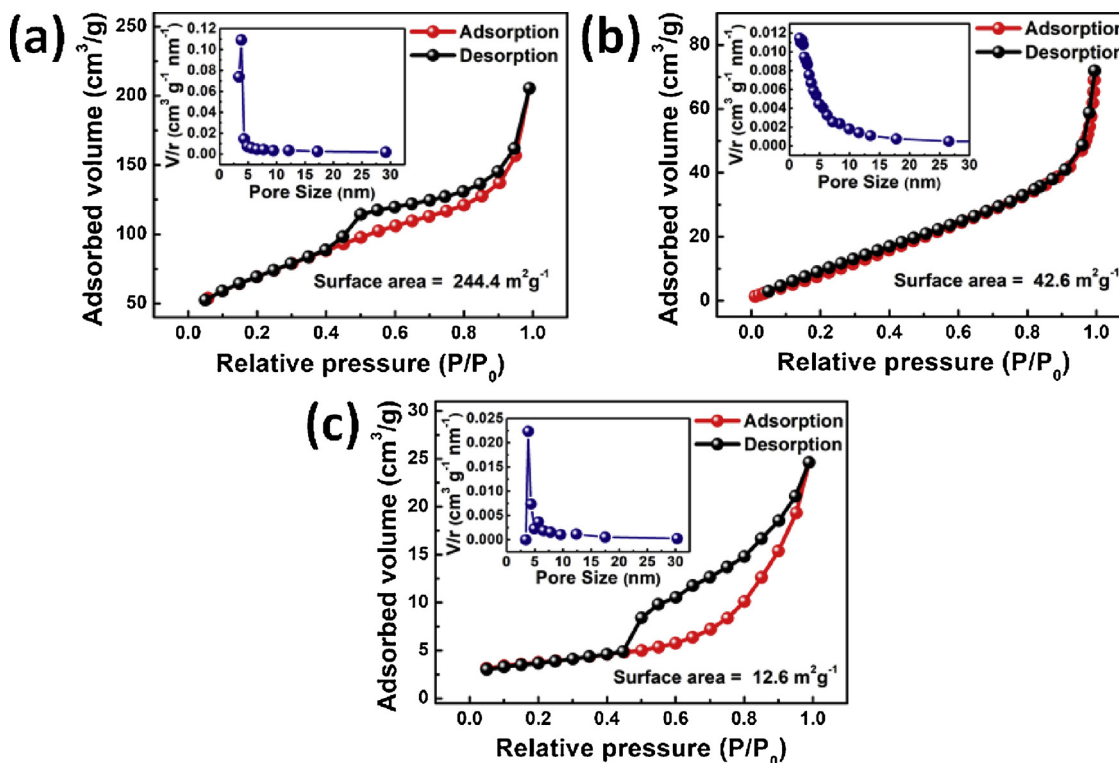
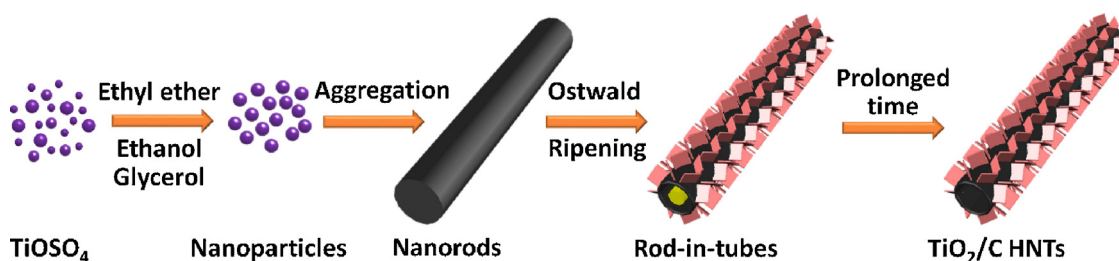


**Fig. 6.** Nitrogen adsorption/desorption isotherms of (a)  $\text{TiO}_2/\text{C}$  HNTs, (b)  $\text{TiO}_2/\text{C}$  NRs and (c)  $\text{TiO}_2/\text{C}$  NPs (inset shows the corresponding BJH pore size distribution curves).

the photocatalyst, facilitates sufficient contact of the catalyst with the reactants, and enhances photocatalytic activity. As seen in the HRTEM images of Fig. 5d, carbon layers are well decorated on the surface of  $\text{TiO}_2$ , which should be conducive to accelerate the separation of electron-hole pairs and enhance the photocatalytic activity of  $\text{TiO}_2/\text{C}$  HNTs. The lattice fringe spacings of 0.35 and 0.32 nm correspond to the (101) plane of anatase  $\text{TiO}_2$  and (110) plane of rutile  $\text{TiO}_2$  respectively (Fig. 5d). This result is consistent with the XRD data as shown in Fig. 1.

Here, we found that the addition of ethyl ether plays a key role in building nanoparticle clusters into rods during the reaction. And the addition of glycerol produce water continuously during the etherifying reactions between alcohol and glycerol to facilitate the dissolution of the core rods and rearrangement of the surface building clusters to form hierarchical tube. When only ethanol as the solvent is added, the nanoparticle building clusters are generated by the alcoholysis reaction between  $\text{TiOSO}_4$  and ethanol and therefore the  $\text{TiO}_2/\text{C}$  NPs show nanoparticle morphology (Scheme 1). When adding ethyl ether and ethanol as the solvent, these nanoparticles aggregate into solid micro-rods, thus the morphology of  $\text{TiO}_2$  turns into nanorods ( $\text{TiO}_2/\text{C}$  NRs) (Scheme 2). Interestingly, when glycerol, ethanol, and ethyl ether as the solvent are added, a hierarchical nanotube morphology with two open ends is formed ( $\text{TiO}_2/\text{C}$  HNTs) (Scheme 3). Because the etherifying reactions take place between alcohol and glycerol produce water

continuously during the solvothermal condition, leading to the dissolution and rearrangement of the surface building clusters [33,34]. In this process, nanosheets are formed and grow at the expense of dissolving the core materials, leading to the formation of the hierarchical hollow structure, and then the  $\text{TiO}_2/\text{C}$  HNTs are obtained (Scheme 3). The evolution pathway of the tube structure structure can be attributed to the well-known asymmetric Ostwald ripening process [35,36].

The surface area and porosity property are two important factors of photocatalysts for water splitting, which were investigated by  $\text{N}_2$ -adsorption/desorption measurements (Fig. 6). The  $\text{N}_2$  adsorption-desorption isotherms of the sample show the typical Langmuir type IV characteristic of a distinct hysteresis loop at high pressure, indicating the presence of mesopores in all the three samples [37]. The BET surface area of the  $\text{TiO}_2/\text{C}$  HNTs is up to  $244.4 \text{ m}^2/\text{g}$ , which is much higher than that of  $\text{TiO}_2/\text{C}$  NRs ( $42.6 \text{ m}^2/\text{g}$ ) and  $\text{TiO}_2/\text{C}$  NPs ( $12.6 \text{ m}^2/\text{g}$ ). The BET surface area of  $\text{TiO}_2/\text{C}$  HNTs also exceeds values of many pristine and carbon-coated  $\text{TiO}_2$  materials in the literature [38,39]. The ultrahigh BET surface area of  $\text{TiO}_2/\text{C}$  HNTs is attributed to its unique hierarchical tube structure. In addition, the pore size analysis based on the isotherms shows that these samples consist of a mesopore distribution in the range 2–5 nm (inset of Fig. 6). Such higher specific surface area with mesoporous structure could provide more photocatalytic active sites, which are expected to significantly improve the

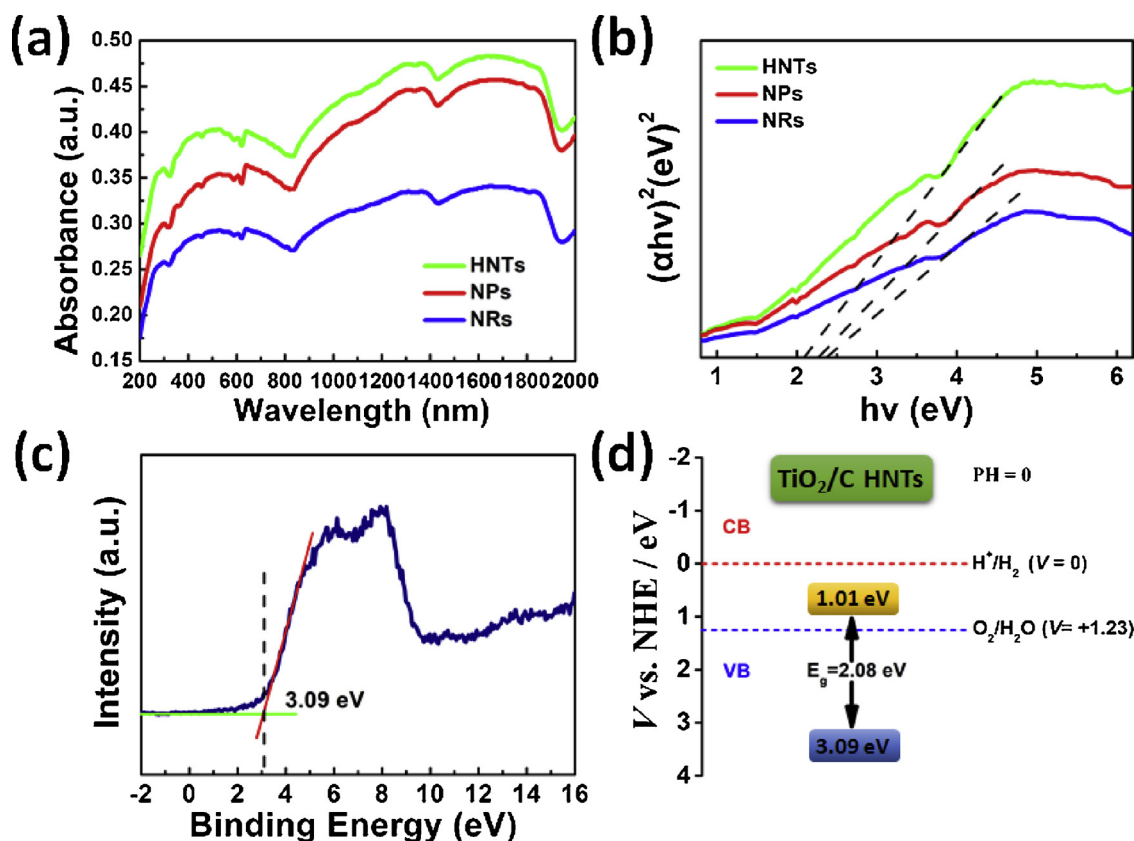
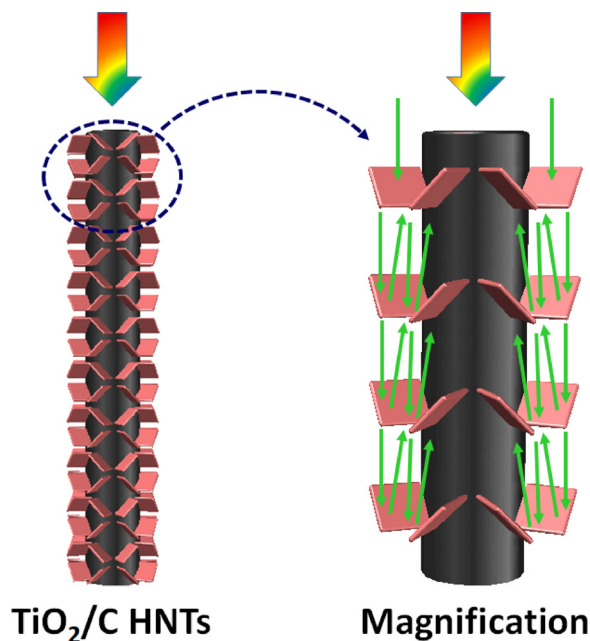


Fig. 7. (a) UV-vis-NIR absorption spectra and (b) band gap values of TiO<sub>2</sub>/C HNTs, TiO<sub>2</sub>/C NPs and TiO<sub>2</sub>/C NRs; (c) XPS valence band of TiO<sub>2</sub>/C HNTs; (d) Schematic illustration of the band structures of TiO<sub>2</sub>/C HNTs.



Scheme 4. Schematic illustrations of light reflecting and scattering within the simplified network of TiO<sub>2</sub>/C HNTs.

photocatalytic properties.

The light absorption properties of TiO<sub>2</sub>/C HNTs, TiO<sub>2</sub>/C NPs and TiO<sub>2</sub>/C NRs were analyzed by UV-vis-NIR absorption spectroscopy. As shown in Fig. S4, pure TiO<sub>2</sub> shows a strong absorption capability in the UV light range. However, the UV-vis-NIR spectrum of TiO<sub>2</sub>/C HNTs, TiO<sub>2</sub>/C NPs and TiO<sub>2</sub>/C NRs exhibit a significantly extended scale

consisting of a visible/NIR light absorption band and an UV absorption band due to the carbon coatings (Fig. 7a). As for various morphology of TiO<sub>2</sub>/C composites, TiO<sub>2</sub>/C HNTs have a higher absorbance capability than that of TiO<sub>2</sub>/C NPs and TiO<sub>2</sub>/C NRs in UV, visible, and NIR light range (Figs. 7a and S5). The increased optical absorption can be attributed to the joint multichannel system formed between metal oxide and carbon [40], as well as a better light trapping properties and reflectance capability of TiO<sub>2</sub>/C HNTs. Such regular hierarchical tube structure with lush nanosheets enables maximizing reflections and scatter efficiency, and thus resulting in multiple absorption of the incident light within the TiO<sub>2</sub>/C HNTs. Herein we propose the possible reflecting and absorbing of light in a simplified pattern of TiO<sub>2</sub>/C HNTs (Scheme 4). It is easy to see that when the light is shined into the hollow tube and lush nanosheets of TiO<sub>2</sub>, it bounces back and forth multiple times and finally be absorbed eventually. This is conducive to more effective photon capturing and thus resulting in an enhancement of light-harvesting efficiency. The band gap energy of TiO<sub>2</sub>/C HNTs, TiO<sub>2</sub>/C NPs and TiO<sub>2</sub>/C NRs could be computed from the formula  $(\alpha h\nu)^2 \propto h\nu - E_g$ , where  $\alpha$ ,  $h$ ,  $\nu$ , and  $E_g$  are absorption coefficient, Planck's constant, light frequency, and band gap energy, respectively (Fig. 7b). Then the estimated  $E_g$  of TiO<sub>2</sub>/C HNTs, TiO<sub>2</sub>/C NPs and TiO<sub>2</sub>/C NRs is about 2.08, 2.37 and 2.26 eV, respectively. Estimating conduction and valence band positions is a conventional way to determine the potential of semiconductor photocatalysts for the reduction and oxidation of water. The XPS valence band spectrum was performed to determine the valence band energies. The valence band (VB) potential of TiO<sub>2</sub>/C HNTs, TiO<sub>2</sub>/C NRs and TiO<sub>2</sub>/C NPs is about 3.09 eV, 2.34 eV and 2.93 eV (Figs. 7c and S6a), respectively, which is below the water oxidation levels ( $V = +1.23$  eV) and is suitable for water oxidation (Figs. 7d and S6b). Furthermore, the calculated VB edge of TiO<sub>2</sub>/C HNTs is more negative than that of TiO<sub>2</sub>/C NRs and TiO<sub>2</sub>/C NPs, indicating the higher oxidation ability of TiO<sub>2</sub>/C HNTs [39].

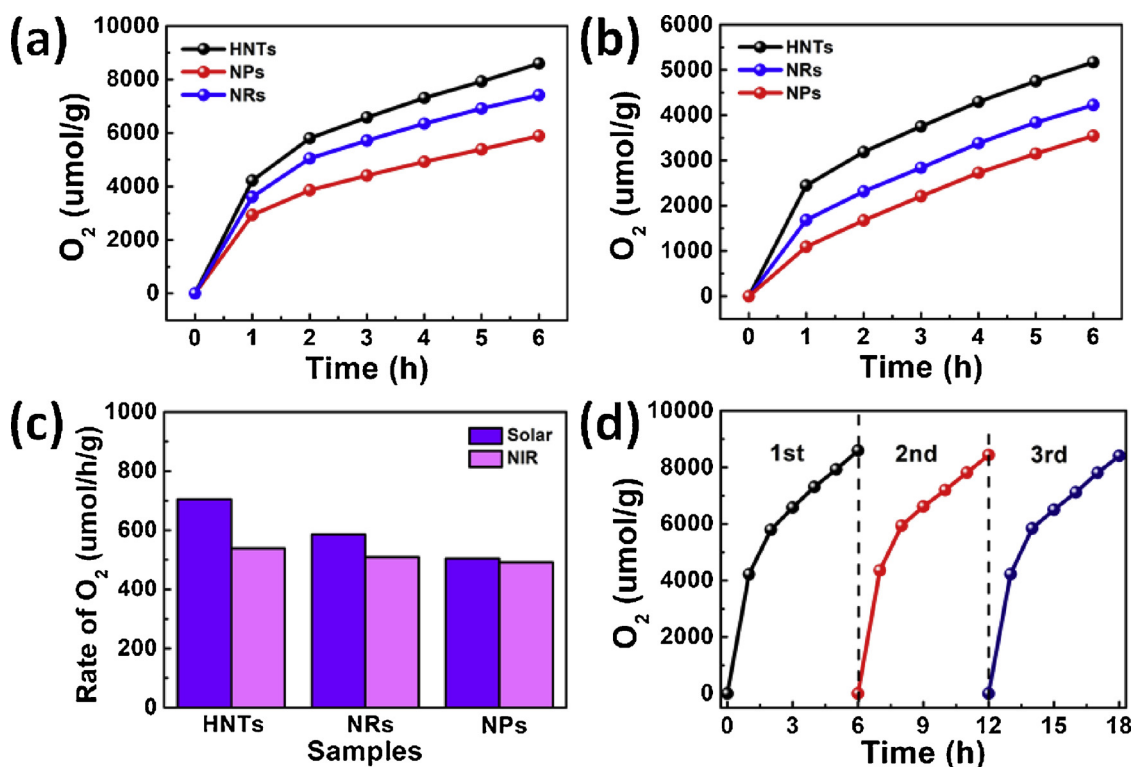


**Fig. 8.** Cumulated evolution of O<sub>2</sub> of TiO<sub>2</sub>/C HNTs, TiO<sub>2</sub>/C NPs and TiO<sub>2</sub>/C NRs under (a) simulated solar light and (b) NIR irradiation; (c) Rate of photocatalytic O<sub>2</sub> production of TiO<sub>2</sub>/C HNTs, TiO<sub>2</sub>/C NPs and TiO<sub>2</sub>/C NRs under simulated solar light and NIR irradiation; (d) Cyclic O<sub>2</sub> evolution curve for the TiO<sub>2</sub>/C HNTs under simulated solar light irradiation.

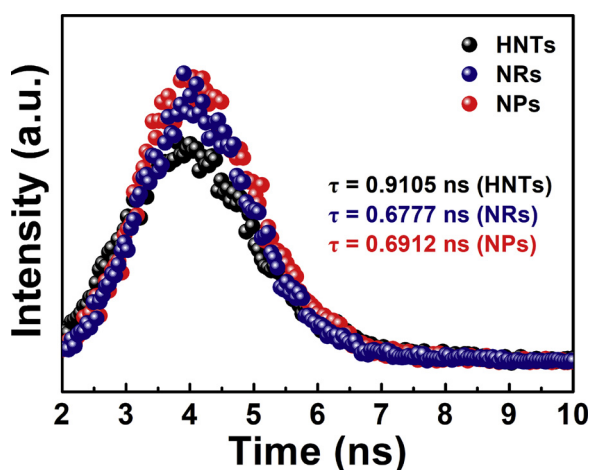


**Fig. 9.** Luminescence decay curves of TiO<sub>2</sub>/C HNTs, TiO<sub>2</sub>/C NPs and TiO<sub>2</sub>/C NRs.

The unique hierarchical nanotube architecture with a high surface area and hollow space as well as full solar spectrum response make TiO<sub>2</sub>/C HNTs highly suitable for photocatalytic applications. The photocatalytic activity toward water splitting over different samples was evaluated by monitoring the time-dependent production of O<sub>2</sub> in simulated solar light ( $\lambda > 200$  nm) and NIR light ( $\lambda > 800$  nm) illuminated catalyst suspensions. As shown in Fig. 8a and c, the TiO<sub>2</sub>/C HNTs exhibit an O<sub>2</sub> generation rate of  $705 \mu\text{mol h}^{-1} \text{g}^{-1}$ , which is far superior to TiO<sub>2</sub>/C NPs ( $585 \mu\text{mol h}^{-1} \text{g}^{-1}$ ) and TiO<sub>2</sub>/C NRs ( $505 \mu\text{mol h}^{-1} \text{g}^{-1}$ ) under simulated solar light irradiation. In order to further confirm the full solar spectrum photocatalytic activity, the photocatalytic activity of O<sub>2</sub> generation under NIR light was evaluated as well (Fig. 8b and c). The O<sub>2</sub> generation rates of 539, 509 and  $491 \mu\text{mol h}^{-1} \text{g}^{-1}$  is obtained for TiO<sub>2</sub>/C HNTs, TiO<sub>2</sub>/C NPs and TiO<sub>2</sub>/C NRs,

respectively. The TiO<sub>2</sub>/C HNTs also display the highest photocatalytic O<sub>2</sub> generation rate under NIR light irradiation. Moreover, the photocatalytic stability of TiO<sub>2</sub>/C HNTs under simulated solar light irradiation was examined upon repeated photoreactions, and no significant decrease in oxygen generation is observed after 18 h (Fig. 8d). Thus, SEM images of TiO<sub>2</sub>/C HNTs after 3 cycles under simulated solar light irradiation are measured (Fig. S7). The photocatalytic stability of the catalyst largely depends on the structural stability of the active materials. As shown in Fig. S7, the interwoven nanosheets on the tube shell are preserved after 3 cycles. The hierarchical tube structure is still maintained, which further confirms the excellent stability of the TiO<sub>2</sub>/C HNTs. We further evaluated the apparent quantum efficiency (AQE) of TiO<sub>2</sub>/C HNTs, TiO<sub>2</sub>/C NPs and TiO<sub>2</sub>/C NRs under visible light irradiation. Table S1 shows the comparison of AQE values over TiO<sub>2</sub>/C HNTs, TiO<sub>2</sub>/C NPs and TiO<sub>2</sub>/C NRs: 3.79% (TiO<sub>2</sub>/C NPs) < 3.86% (TiO<sub>2</sub>/C NRs) < 4.03% (TiO<sub>2</sub>/C HNTs). Thus, the TiO<sub>2</sub>/C HNTs present the highest AQE value. The results demonstrate that TiO<sub>2</sub>/C HNTs can serve as a promising photocatalyst for O<sub>2</sub> evolution from water, with high activity and excellent recyclability. Therefore, the efficient and stable full solar spectrum-driven-oxygen evolution is realized on TiO<sub>2</sub> hierarchical nanotubes for the first time with carbon coating. The wavelength-dependent activity (Fig. S8) also confirms that the TiO<sub>2</sub>/C HNTs ensure a better photocatalytic O<sub>2</sub> generation activity in 400–1000 nm, in good agreement with the DRS analysis (Fig. 7a).

The recombination of photo-generated electrons and holes cause the fluorescence lifetime decay rapidly [41]. We further tested the photo-excited charge carriers lifetimes properties of TiO<sub>2</sub>/C HNTs, TiO<sub>2</sub>/C NRs and TiO<sub>2</sub>/C NPs by using the time-resolved fluorescence decay spectra. As shown in Fig. 9, by fitting the fluorescence lifetime decay curve, it is concluded that all three samples are single exponential decay. The lifetimes  $\tau$  obtained for TiO<sub>2</sub>/C HNTs, TiO<sub>2</sub>/C NRs and TiO<sub>2</sub>/C NPs are 0.9105 ns, 0.6777 ns and 0.6912 ns, respectively. The extension of the trapped carrier lifetimes in TiO<sub>2</sub>/C HNTs indicate the advantages of the hierarchical tube structure with multi-channels for



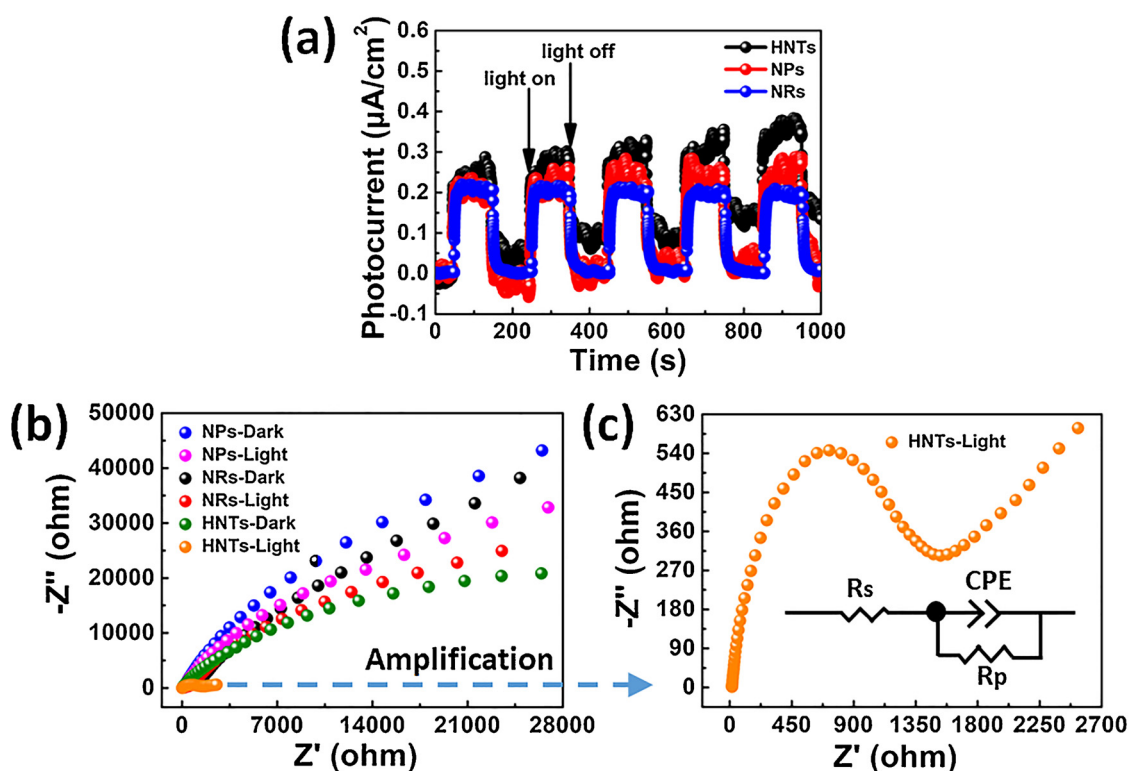
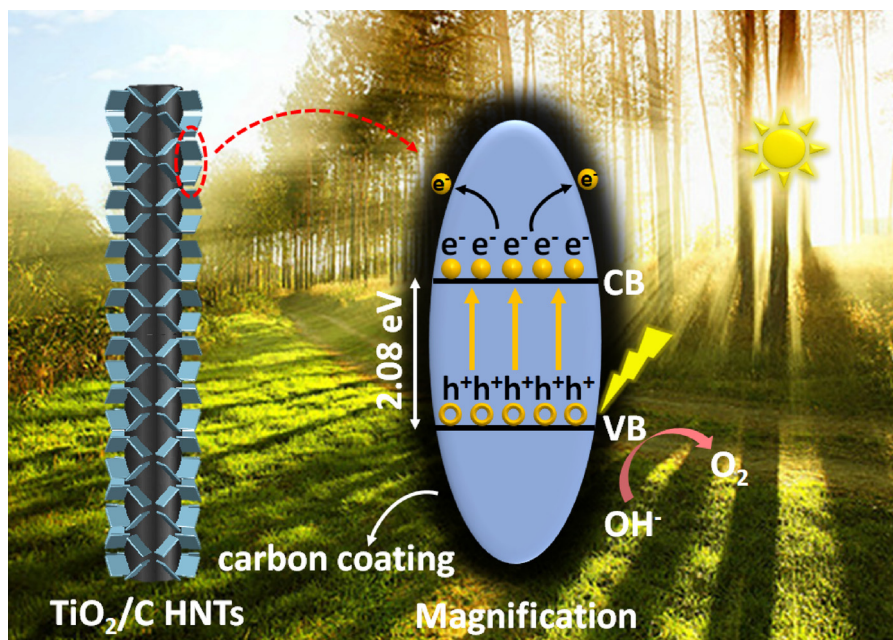


Fig. 10. (a) The transient photocurrent density and (b, c) the electrochemical impedance spectra (EIS) of the samples (The inset is the equivalent circuit diagram).



Scheme 5. Schematic of the photocatalytic mechanism of  $\text{TiO}_2/\text{C}$  HNTs under full solar spectrum light.

charge transfer, which promotes the electron-hole separation and hinders their efficient recombination.

The photoelectrochemical (PEC) analysis has been performed to investigate the charge carrier separation and transfer process of the  $\text{TiO}_2/\text{C}$  HNTs,  $\text{TiO}_2/\text{C}$  NPs and  $\text{TiO}_2/\text{C}$  NRs, which are closely related to the performance of photocatalysts [42]. Fig. 10a shows a comparison of the photocurrent-time (I-t) curves for  $\text{TiO}_2/\text{C}$  HNTs,  $\text{TiO}_2/\text{C}$  NRs and  $\text{TiO}_2/\text{C}$  NPs samples with typical on-off cycles of intermittent simulated solar light irradiation. Notably, the fast photocurrent transient responses for on-off cycles could be observed, and it can be clearly seen

that the photocurrent value of  $\text{TiO}_2/\text{C}$  HNTs composite is higher than that of  $\text{TiO}_2/\text{C}$  NRs and  $\text{TiO}_2/\text{C}$  NPs, indicating the recombination of charge carrier will be efficiently reduced (Fig. 10a). The increase of photocurrent intensity could be ascribed to the efficient carrier transfer and separation process. The introduction of carbon coating not only plays an important role in the improvement of visible or even NIR absorption, but also serves as an electron mediator, inhibiting the recombination of photoinduced electrons and holes effectively. As illustrated in Fig. 10b and c, the charge transfer ability of  $\text{TiO}_2/\text{C}$  HNTs,  $\text{TiO}_2/\text{C}$  NRs and  $\text{TiO}_2/\text{C}$  NPs samples were conducted by

electrochemical impedance (EIS) measurements. In general, a smaller arc radius on an EIS Nyquist plot means a smaller charge-transfer resistance ( $R_p$ , the inset of Fig. 10c) on the electrode surface and a higher separation efficiency of electron-hole pairs [43]. Obviously, the impedance values of samples especially the  $\text{TiO}_2/\text{C}$  HNTs in the dark are significantly larger than those under light illumination, which is attributable to increased electron conductivity under light illumination. Furthermore, as shown in Fig. 10b and c, the arc size for the samples under light irradiation are  $\text{TiO}_2/\text{C}$  HNTs <  $\text{TiO}_2/\text{C}$  NRs <  $\text{TiO}_2/\text{C}$  NPs, suggesting that the  $\text{TiO}_2/\text{C}$  HNTs owns the most effective separation of photogenerated charges. Apparently, there is well agreement among transient PL and photocurrent results, validating that the  $\text{TiO}_2/\text{C}$  HNTs would obviously improve the charge transfer rate. Thus, the improved transfer efficiency of charge carriers could lead to the enhanced photocatalytic activity of  $\text{TiO}_2/\text{C}$  HNTs materials.

A schematic of the proposed photocatalytic mechanism of  $\text{TiO}_2/\text{C}$  HNTs under full solar spectrum light is provided (Scheme 5). The photoexcited electrons in the CB of  $\text{TiO}_2$  nanotubes could migrate into the carbon coatings, leading to an efficient spatial separation of electrons and holes. The resulting depression of electron-hole recombination is consistent with the extension of the trapped carrier lifetimes (Fig. 9), as previously discussed. Therefore, the mesoporous hierarchical hollow tube structure of  $\text{TiO}_2/\text{C}$  HNTs with strong electron acceptor, excellent visible/NIR response coupling and large specific area facilitate the charge separation and consequently induce highly efficient generation of  $\text{O}_2$  under full solar spectrum light.

#### 4. Conclusions

Herein, we report an unprecedented strategy for the rational design of carbon coated hierarchical  $\text{TiO}_2$  nanotubes ( $\text{TiO}_2/\text{C}$  HNTs) as efficient full solar spectrum light photocatalysts for water oxidation. The formation of the hierarchical tube structure follows an asymmetric Ostwald ripening mechanism. This unique  $\text{TiO}_2/\text{C}$  HNTs have increased full solar spectrum absorption capability, high BET area of  $244.4 \text{ m}^2 \text{ g}^{-1}$ , mesoporous structure, and long fluorescence lifetimes of 0.91 ns. The  $\text{TiO}_2/\text{C}$  HNTs show much higher  $\text{O}_2$  production rate than that of  $\text{TiO}_2/\text{C}$  NPs and  $\text{TiO}_2/\text{C}$  NRs, and excellent stability. The presence of carbon coatings on the surface reduces the band gap and provides light absorption in the visible and NIR region, facilitating electron-hole separation. The unique hierarchical nanotube structure further increase the specific surface area and light-harvesting efficiency, which significantly enhance the photocatalytic performance. The present finding that  $\text{TiO}_2/\text{C}$  HNTs acted as an efficient full solar spectrum water oxidation photocatalyst is the first example of a Ti-based photocatalyst.

#### Acknowledgements

The authors are thankful for fundings from the National Natural Science Foundation of China (No. 51872173), Natural Science Foundation of Shandong Province (No. ZR2017JL020), Taishan Scholarship of Climbing Plan (No. tspd20161006), and Key Research and Development Program of Shandong Province (No. 2018GGX102028).

#### Appendix A. Supplementary data

Supplementary material related to this article can be found, in the

online version, at doi:<https://doi.org/10.1016/j.apcatb.2018.11.017>.

#### References

- [1] L. Zhang, C. Yang, Z. Xie, X. Wang, Appl. Catal. B: Environ. 224 (2018) 88–894.
- [2] J. Di, C. Chen, C. Zhu, M. Ji, J. Xia, C. Yan, W. Hao, S. Li, H. Li, Z. Liu, Appl. Catal. B: Environ. 238 (2018) 119–125.
- [3] X. Zhang, Y. Guo, J. Tian, B. Sun, Z. Liang, X. Xu, H. Cui, Appl. Catal. B: Environ. 232 (2018) 355–364.
- [4] L. Yu, Y. Ding, M. Zheng, Appl. Catal. B: Environ. 209 (2017) 45–52.
- [5] J. Chen, C. Dong, D. Zhao, Y. Huang, X. Wang, L. Samad, L. Dang, M. Shearer, S. Shen, L. Guo, Adv. Mater. 29 (2017) 1606198.
- [6] A. Das, Z. Han, W.W. Brennessel, P.L. Holland, R. Eisenberg, ACS Catal. 5 (2015) 1397–1406.
- [7] A.R. Parent, R.H. Crabtree, G.W. Brudvig, Chem. Soc. Rev. 42 (2013) 2247–2252.
- [8] M. Murakami, D. Hong, T. Suenobu, S. Yamaguchi, T. Ogura, S. Fukuzumi, J. Am. Chem. Soc. 133 (2011) 11605–11613.
- [9] K. Nakata, A. Fujishima, J. Photochem. Photobiol. C 13 (2012) 169–189.
- [10] F. Vaquero, R.M. Navarro, J.L.G. Fierro, Appl. Catal. B: Environ. 203 (2017) 753–767.
- [11] M. Ge, Q. Li, C. Cao, J. Huang, S. Li, S. Zhang, Z. Chen, K. Zhang, S.S. Al-Deyab, Y. Lai, Adv. Sci. 4 (2017) 1600152.
- [12] L.K. Preethi, T. Mathews, M. Nand, S.N. Jha, C.S. Gopinath, S. Dash, Appl. Catal. B: Environ. 218 (2017) 9–19.
- [13] J.F. Brito, F. Tavella, C. Genovese, C. Ampelli, M.V.B. Zanoni, G. Centi, S. Perathoner, Appl. Catal. B: Environ. 224 (2018) 136–145.
- [14] Y.H. Chiu, Y.J. Hsu, Nano Energy 31 (2017) 286–295.
- [15] X. Wang, A. Wang, M. Lu, J. Ma, Chem. Eng. J. 337 (2018) 372–384.
- [16] S. Li, J. Chen, F. Zheng, Y. Li, F. Huang, Nanoscale 5 (2013) 12150.
- [17] L. Gao, Y. Li, J. Ren, S. Wang, R. Wang, G. Fu, Y. Hu, Appl. Catal. B: Environ. 202 (2017) 127–133.
- [18] Y. Yang, G. Liu, J.T.S. Irvine, H. Cheng, Adv. Mater. 28 (2016) 5850–5856.
- [19] N. Guo, Y. Zeng, H. Li, X. Xu, H. Yu, X. Han, J. Hazard. Mater. 353 (2018) 80–88.
- [20] J. Jin, C. Wang, X. Ren, S. Huang, M. Wu, L. Chen, T. Hasan, B. Wang, Y. Li, B. Su, Nano Energy 38 (2017) 118–126.
- [21] A. Ziarati, A. Badieli, R. Luque, W. Ouyang, J. Mater. Chem. A 6 (2018) 8962–8968.
- [22] R. Li, Y. Weng, X. Zhou, X. Wang, Y. Mi, R. Chong, H. Han, C. Li, Energy Environ. Sci. 8 (2015) 2377–2382.
- [23] Y. Li, Y. Xue, J. Tian, X. Song, X. Zhang, X. Wang, H. Cui, Solar Energy Mater. Solar Cells 168 (2017) 100–111.
- [24] C. Marchal, T. Cottineau, M.G. Méndez-Medrano, Adv. Energy Mater. 8 (2018) 1702142.
- [25] X. Hu, H. Zhao, J. Tian, J. Gao, Y. Li, H. Cui, Solar Energy Mater. Solar Cells 172 (2017) 108–116.
- [26] A. Zhang, W. Wang, J. Chen, C. Liu, Q. Li, X. Zhang, W. Li, Y. Si, H. Yu, Energy Environ. Sci. 11 (2018) 1444–1448.
- [27] A. Miyoshi, S. Nishioka, K. Maeda, Chem. Eur. J. 24 (2018) 1–17.
- [28] K. Yang, Y. Dai, B. Huang, M. Whangbo, J. Phys. Chem. C 113 (2009) 2624–2629.
- [29] F. Dong, S. Guo, H. Wang, X. Li, Z. Wu, J. Phys. Chem. C 115 (2011) 13285–13292.
- [30] Y. Zhang, C. Wang, H.S. Hou, G.Q. Zou, X.B. Ji, Adv. Energy Mater. 7 (2017) 1600173.
- [31] J. Chen, G.Q. Zou, H.S. Hou, Y. Zhang, Z. Huang, X.B. Ji, J. Mater. Chem. A 4 (2016) 12591.
- [32] H. He, Q. Gan, H. Wang, G. Xu, X. Zhang, D. Huang, F. Fu, Y. Tang, K. Amine, M. Shao, Nano Energy 44 (2018) 217–227.
- [33] H. Li, Z. Bian, J. Zhu, D. Zhang, G. Li, Y. Huo, H. Li, Y. Lu, J. Am. Chem. Soc. 129 (2007) 8406–8407.
- [34] X. Yin, C. Li, M. Zhang, Q. Hao, S. Liu, L. Chen, T. Wang, J. Phys. Chem. C 114 (2010) 8084–8088.
- [35] L. Larini, D. Leporini, J. Chem. Phys. 123 (2005) 144907.
- [36] Y. Zhang, C. Wang, H. Hou, G. Zou, X. Ji, Adv. Energy Mater. 7 (2017) 1600173.
- [37] H. He, H. Wang, D. Sun, M. Shao, X. Huang, Y. Tang, Electrochim. Acta 236 (2017) 43–52.
- [38] T. Jia, F. Fu, D. Yu, J. Cao, G. Sun, Appl. Surf. Sci. 430 (2018) 438–447.
- [39] X. Hu, X. Liu, J. Tian, Y. Li, H. Cui, Catal. Sci. Technol. 7 (2017) 4193–4205.
- [40] J. Hu, L. Wang, P. Zhang, C. Liang, G. Shao, J. Power Sources 328 (2016) 28–36.
- [41] Y. Li, X. Deng, J. Tian, Z. Liang, H. Cui, Appl. Mater. Today 13 (2018) 217–227.
- [42] Y. Shang, F. Niu, S. Shen, Chin. J. Catal. 39 (2018) 502–509.
- [43] X. Hu, S. Lu, J. Tian, N. Wei, X. Song, X. Wang, H. Cui, Appl. Catal. B: Environ. 24 (2019) 329–337.